

New Metal-Organic Systems with a Functionalized Oxamate-Type Ligand and Mn^{II}, Fe^{II}, Cu^{II} and Zn^{II}

Jhonny W. Maciel,^a Lucas H. G. Kalinke,^{a,b} Ana K. Valdo,^a Felipe T. Martins,^a Renato Rabelo,^c Nicolás Moliner,^c Joan Cano,^b Miguel Julve,^{*,c} Francesc Lloret^c and Danielle Cangussu^{†*,a}

^aInstituto de Química, Universidade Federal de Goiás, 74001-970 Goiânia-GO, Brazil

^bInstituto Federal de Goiás, Campus Anápolis, 75131-457 Anápolis-GO, Brazil

^cDepartament de Química Inorgànica, Institut de Ciència Molecular (ICMol), C/ Catedrático José Beltrán 2, 46980 Paterna, Valencia, Spain

Four new complexes of formula [Fe(H₂pcpa)₂(H₂O)₂] (**1**), {[Mn(Hpcpa)(H₂O)₃]·1/2H₂O}_n (**2**), {[Zn(Hpcpa)(H₂O)₃]·1/2H₂O}_n (**3**) and [Cu₂(Hpcpa)₂(bipy)₂]·8H₂O (**4**) [H₃pcpa = *N*-(4-carboxyphenyl) oxamic acid; bipy = 2,2'-bipyridine] have been synthesized and their structures determined by X-ray diffraction. The structure of **1** consists of mononuclear iron(II) units where each iron(II) ion is six-coordinate by two *trans*-positioned water molecules and two bidentate H₂pcpa⁻ ligands building a distorted octahedral environment. **2** and **3** consist of neutral zigzag chains of Mn^{II} and Zn^{II} ions respectively, the Hpcpa²⁻ groups acting as linkers in a bidentate/monodentate coordination mode with three *mer*-positioned water molecules achieving the six-coordination around the metal centers. Compound **4** is a neutral centrosymmetric dicopper(II) complex where two Hpcpa²⁻ groups adopting the bidentate/monodentate coordination mode and act as bridges and bidentate bipy molecules act as end-cap ligands, describing a square pyramidal surrounding around each copper atom. Cryomagnetic measurements for **1**, **2** and **4** in the temperature range 1.9-300 K reveal the occurrence of a field-induced single-ion magnet (SIM) behavior (**1**) and weak interchain ($J = -0.22$ cm⁻¹, **2**) and intradimer ($J = -0.39$ cm⁻¹, **4**) antiferromagnetic interactions, the Hamiltonian being defined as $H = -J S_a S_b$.

Keywords: iron(II), manganese(II), zinc(II), copper(II), oxamate, magnetic properties, single-ion magnet

Introduction

The metallosupramolecular chemistry is nowadays a multidisciplinary research field where the design and synthesis of a great variety of supramolecular structures with interesting properties such as electrochemistry, photophysics, catalysis and magnetism has been achieved.¹ A great interest was developed in molecular magnetism for the rational design of ligands capable of stepwise assembling metal ions to yield prefixed polynuclear arrays.²⁻⁵ Selected examples in this respect are oxalate⁶⁻¹⁹ and substituted oxamate- and oxamidate-type ligands (see Figure 1).²⁰⁻²² These ligands are able to mediate strong magnetic interactions between the paramagnetic metal ions which are linked by them.²³ The variety of the R substituent

on the oxamate (oxamidate) group is at the origin of the great versatility of these substituted ligands envisaging the preparation of multifunctional supramolecular structures, as shown in the last years.²⁴⁻³¹

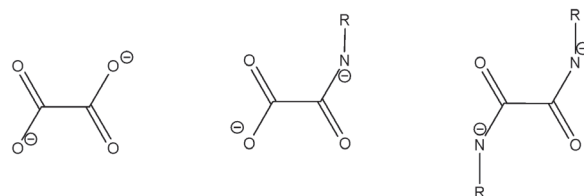


Figure 1. Oxalate (left), monosubstituted oxamate (middle) and disubstituted oxamidate (right).

Among the different choices of the R group, we will focus first on some achievements with the monoxamate family where R is a phenyl group of a phenyl-substituted derivative. The first generation

*e-mail: miguel.julve@uv.es; danielle_cangussu@ufg.br

of this family is represented by *N*-phenyloxamate (dianion of *N*-phenyloxamic acid, H₂pma) and its methyl-substituted analogues *N*-2-methylphenyloxamic acid (H₂Mepma), *N*-2,6-dimethylphenyl oxamic acid (H₂Me₂pma) and *N*-2,4,6-trimethylphenyloxamic acid (H₂Me₃pma). The heterobimetallic chains of general formula [M^{II}Cu^{II}(Me_xpma)₂(H₂O)_y(DMSO)_z]_n (M = Mn and Co; x = 2 and 3; DMSO = dimethyl sulfoxide) were obtained, those with cobalt(II) exhibiting slow relaxation of magnetization, that is single chain magnet (SCM) behavior.^{32,33} Also mononuclear bis(*N*-substituted oxamato) palladate(II) complexes with methyl-, methoxy-, and halo-substituents on the phenyl ring of the *N*-phenyloxamate have been shown to be efficient and environmentally friendly catalysts in palladium catalyzed Suzuki and Heck reactions by using aryl halides in ionic liquids.³⁴⁻³⁷ Interestingly, the elusive [Pd(H₂O)₄]²⁺ species which is considered a reaction intermediate for the nitrile hydration was trapped together with the acetamide molecule during an oxamate-palladate(II) complexation as illustrated by the X-ray structure of the compound (*n*-Bu₄N)₄[Pd(H₂O)₄][Pd(4-Xpma)₂]₃·2CH₃CONH₂ (*n*-Bu₄N⁺ = tetra-*n*-butylammonium cation; X = Cl and Br).³⁸

Aiming at improving the coordinating possibilities of the *N*-phenyloxamate ligand, some of us prepared the *N*-(4-carboxyphenyl)oxamic acid (H₃pcpa) and started a systematic study of its complexing ability towards transition metal ions. The first attempts yielded the cobalt(II) chain of formula {[Co(Hpcpa)(H₂O)₃]_n·3/2nH₂O} and the dicopper(II) complex [Cu₂(MeHpcpa)₄(MeOH)₂] (MeHpcpa⁻ = monoanion of the methyl ester derivative of the H₃pcpa).³⁹ The Hpcpa²⁻ ligand exhibits a bidentate/monodentate bridging mode in the former compound whereas only the carboxylate group in the *syn-syn* bridging mode of the MeHpcpa⁻ ligand is involved in the second one, the monoprotonated methyl oxamate fragment remaining uncoordinated. As an extension of this work, we present here the synthesis and X-ray structures of the compounds of formula [Fe(H₂pcpa)₂(H₂O)₂] (**1**), {[Mn(Hpcpa)(H₂O)₃]_n·1/2H₂O} (**2**), {[Zn(Hpcpa)(H₂O)₃]_n·1/2H₂O} (**3**) and [Cu₂(Hpcpa)₂(bipy)₂]_n·8H₂O (**4**) (bipy = 2,2'-bipyridine) together with the variable-temperature magnetic study of **1**, **2** and **4**.

Experimental

Materials and methods

Iron(III) chloride hydrate, manganese(II) chloride tetrahydrate, zinc(II) chloride, copper(II) nitrate trihydrate,

copper(II) chloride dihydrate, sodium hydroxide, triethylamine, ethyl oxalyl chloride and 4-aminobenzoic acid were purchased from Sigma-Aldrich (Goiânia, Brazil) and used as received. The monoethyl ester derivative of the *N*-(4-carboxyphenyl)oxamic acid (EtH₂pcpa) was prepared by reacting ethyl oxalyl chloride with 4-aminobenzoic acid and triethylamine in 1:1:1 molar ratio under reflux at 80 °C during four hours, the general procedure previously described for these type of ligands.⁴⁰⁻⁴² Na₂Hpcpa was prepared by treatment of the Et₂H₂pcpa proligand with aqueous NaOH (1:2.1 proligand to base molar ratio) at 65 °C for 30 min under vigorous stirring. The sodium salt was obtained as a white solid after reducing the volume of the resulting solution under gentle heating. The precipitate was collected by filtration, washed with small amounts of cold water, and air-dried. The compound [Cu(NO₃)(bipy)(H₂O)₃](NO₃) was prepared as reported in the literature.⁴³ Elemental analysis (C, H, N) were conducted by the Microanalytical Service of the Federal University of Goiás and the metal contents was determined by spectrophotometry with a Hitachi-Z8200 spectrophotometer.

Preparation of complexes

Synthesis of [Fe(H₂pcpa)₂(H₂O)₂] (**1**)

X-ray quality crystals of **1** were grown by slow diffusion in an H-shaped tube of an aqueous solution of Na₂Hpcpa (0.10 mmol, 1.0 cm³) on one arm and another aqueous solution of iron(III) chloride (0.10 mmol, 1.0 cm³) at the other arm. Water was slowly added to fill the H-tube and after being covered with parafilm, it was allowed to diffuse at 30 °C. Orange/brown plates of **1** were formed after twenty days. They were collected and dried on filter paper under ambient conditions. Yield 24%; anal. data for **1** (C₁₈H₁₆N₂O₁₂Fe, MW = 508.18 g mol⁻¹) calcd.: C 42.54, H 3.17, N 5.51, Fe 11.01, found: C 42.33, H 3.10, N 5.45, Fe 10.90%; IR (KBr) ν / cm⁻¹ 3415, 3360, 1687, 1670, 1603, 1590, 1543, 1427, 1380, 1360, 1310, 1292, 773, 698.

Synthesis of {[Mn(Hpcpa)(H₂O)₃]_n·1/2H₂O} (**2**) and {[Zn(Hpcpa)(H₂O)₃]_n·1/2H₂O} (**3**)

Colourless plates of **2** and **3** were grown by the same method used for **1**, the starting aqueous solutions being Na₂Hpcpa (0.10 mmol, 1.0 cm³) and the manganese(II) or zinc(II) as chloride salts (0.10 mmol, 1.0 cm³) for **2** and **3**, respectively. Yield 42% (**2**) and 62% (**3**); anal. data for **2** (C₁₈H₂₄N₂O₁₇Mn₂, MW = 650.27 g mol⁻¹); calcd.: C 33.14, H 4.02, N 4.29, Mn 8.46, found: C 33.02, H 3.90, N 4.32, Mn 8.35%; IR (KBr) ν / cm⁻¹ 3600-3200, 1667, 1610, 1581, 1537, 1424, 1362, 791, 780, 697. Anal. data for **3**

$C_{18}H_{24}N_2O_{17}Zn_2$ (MW = 671.17 g mol⁻¹) calcd.: C 32.12, H 3.89, N 4.16, Zn 9.83, found: C 31.96, H 3.72, N 4.09, Zn 9.75%; IR (KBr) ν / cm⁻¹ 3600-3200, 1667, 1611, 1580, 1540, 1423, 1360, 793, 781, 698.

Synthesis of [Cu₂(Hpcpa)₂(bipy)₂]₂·8H₂O (**4**)

Blue prisms of **4** were also grown after twenty days by slow diffusion in an H-shaped tube containing an aqueous solution of Na₂Hpcpa (0.1 mmol, 1.0 cm³) on one arm and [Cu(NO₃)(bipy)(H₂O)₃]₂NO₃ (0.2 mmol, 1.0 cm³) at the other arm. They were collected and dried on filter paper at the open air. Yield 74%; anal. data for **4** (C₃₈H₄₂N₆O₁₈Cu₂, MW = 997.88 g mol⁻¹), calcd.: C 46.81, H 3.93, N 8.80, Cu 6.41, found: C 46.60, H 3.91, N 8.65, Cu 6.35%; IR (KBr) ν / cm⁻¹ 3650-3100, 1684, 1636, 1602, 1594, 1538, 1540, 1447, 1359, 739, 771, 731, 699.

Physical techniques

Infrared spectra of **1-4** were recorded with a PerkinElmer Spectrum 400 FT-IR/FT-FIR spectrophotometer as KBr pellets in the range 4000-400 cm⁻¹. Diffuse reflectance spectra of **1**, **2** and **4** were performed in a PerkinElmer Lambda 900 UV/Vis/NIR in the 250-2500 nm region. X-ray powder diffraction data were collected for polycrystalline powders of **1-4** on an Empyrean PANalytical powder diffractometer, using Cu-K α radiation (λ = 1.54177 Å) at a voltage of 45 kV and a current of 40 mA in the 2 θ range 3.00-50.00° with step-size of 0.0131°. Variable-temperature (1.9-300 K) direct current (dc) magnetic susceptibility measurements under applied dc fields of 0.1 T ($T \geq 50$ K) and 500 G ($T < 50$ K) and variable-field (0-5 T) magnetization measurements at 2.0 K were carried out on crushed crystals of **1**, **2** and **4** by means of a Quantum Design SQUID magnetometer. Alternating current (ac) magnetic susceptibility measurements on a sample of **1** were done with a Quantum Design Physical Property Measurement System (PPMS) under different applied dc fields in the temperature range 2.0-12 K. The corrections for the diamagnetism of the constituent atoms were estimated from Pascal's constants⁴⁴ as 231×10^{-6} (**1**), 153×10^{-6} (**2**) and 522×10^{-6} cm³ mol⁻¹ K (**4**) (*per* one iron(II) (**1**) / manganese(II) (**2**) and two copper(II) (**4**) ions). Corrections for the temperature independent paramagnetism (60×10^{-6} cm³ mol⁻¹ *per* mol of copper(II) ions) (**4**) and the magnetization of the sample holder (**1**, **2** and **4**) were also applied.

Computational details

In order to evaluate the parameters that determine

the axial (*D*) and rhombic (*E*) zero-field splitting (zfs), calculations based on the second order N-electron valence state perturbation theory (CASSCF/NEVPT2) applied on the wave function, which was previously obtained from the complete active space (CAS) calculation, were performed on the structurally characterized molecular geometry of the high-spin iron(II) complex (**1**). The calculations were carried out with the version 4.0 of the ORCA programme⁴⁵ using the TZVP basis set proposed by Ahlrichs and co-workers^{46,47} and the auxiliary TZV/C Coulomb basis sets.⁴⁸⁻⁵⁰ The contributions to zfs from 5 quintets and 20 triplet excited states generated from an active space with six electrons in five 3d orbitals were included using the approach of the 2nd order spin-orbit coupling (SOC).

X-ray crystallography data collection and refinement

Single-crystals of **1-4** were mounted on a Bruker-AXS Kappa Duo diffractometer to measure the intensity data at room temperature by using CuK α radiation. Each single-crystal was selected out from individual crystallization batches. The diffraction frames were recorded by φ and ω scans using APEX2,⁵¹ and raw dataset treatment was performed using the programs SAINT and SADABS.⁵¹ Multi-scan absorption correction has been employed to all datasets.⁵² The structures were solved by direct methods with SHELXS-2014,⁵³ wherein C, O, N, Mn, Fe, Cu and Zn were readily assigned from the Fourier map. All full-matrix refinements were performed on F^2 using SHELXL-2014.⁵³ Hydrogen atoms were stereochemically positioned and refined with fixed individual isotropic displacement parameters (U_{iso}) and equivalent isotropic displacement parameter (U_{eq}) [$U_{iso}(H) = 1.2U_{eq}(C_{aromatic}$ and N) or $1.5U_{eq}(O)$] using a riding model with fixed bond lengths of 0.93 Å (C–H, aromatic), 0.86 Å (N–H) 0.82 Å (O–H, hydroxyl) and 0.84 Å (O–H in water). The Mercury⁵⁴ and ORTEP3⁵⁵ programs were used within the WinGX⁵⁵ software package to prepare artwork representations. Chimera⁵⁶ was also employed to prepare illustrations. Residual electron density peaks close to the metal center were observed in the structures **2** and **4** even after the absorption correction. This led to high value for residual electron density peaks and consequently to high *R*1 and *wR*2 in statistics. Crystallographic data and refinement parameters of **1** to **4** are summarized in Table 1. Selected bond lengths and angles and the hydrogen bonds for all the compounds are grouped in Tables 2 and S1 (Supplementary Information (SI) section), respectively. All crystallographic data are available in the SI section as CIF files. CCDC numbers are 1869708 (**1**), 1869709 (**2**), 1869710 (**3**) and 1869711 (**4**).

Table 1. Crystal data and refinement statistics for the compounds **1-4**

		1	2	3	4
Chemical formula		C ₁₈ H ₁₆ N ₂ O ₁₂ Fe	C ₁₈ H ₂₄ N ₂ O ₁₇ Mn ₂	C ₁₈ H ₂₄ N ₂ O ₁₇ Zn ₂	C ₃₈ H ₄₂ N ₆ O ₁₈ Cu ₂
Formula weight / (g mol ⁻¹)		508.18	650.27	671.17	997.88
Crystal system		triclinic	orthorhombic	orthorhombic	triclinic
Space group		P-1	Pbcn	Pbcn	P-1
Z		1	4	4	1
Temperature / K		296(2)	296(2)	296(2)	296(2)
Unit cell dimensions	<i>a</i> / Å	4.8094(4)	11.6109(4)	9.9959(15)	8.1399(11)
	<i>b</i> / Å	5.9688(7)	7.3054(3)	12.6546(18)	9.9959(15)
	<i>c</i> / Å	17.5936(10)	28.1064(10)	77.108(10)	12.6546(18)
	α / degree	81.032(7)	90	88.005(10)	77.108(10)
	β / degree	82.702(6)	90	87.143(9)	88.005(10)
	γ / degree	82.265(8)	90	1002.2(3)	87.143(9)
Volume / Å ³		491.42(8)	2384.05(15)	2312.41(14)	1002.2(3)
ρ_{calc} / (g cm ⁻³)		1.717	1.812	1.928	1.653
Absorption coefficient μ / mm ⁻¹		6.842	9.454	3.413	2.085
Absorption correc. (multi-scan) T _{min} /T _{max}		0.392/0.578	0.290/0.623	0.652/0.843	0.344/0.904
θ range for data collection / degree		7.693-66.426	3.145-66.574	3.172-66.495	3.584-66.464
Index ranges	<i>h</i>	-5 to 5	-13 to 9	-13 to 11	-9 to 5
	<i>k</i>	-5 to 7	-7 to 8	-8 to 8	-11 to 11
	<i>l</i>	-20 to 20	-32 to 31	-33 to 31	-14 to 14
Data collected		2257	5711	5004	5951
Unique reflections		1587	2011	1890	3200
Symmetry factor (<i>R</i> _{int})		0.0360	0.0477	0.0272	0.0913
Completeness to θ_{max} / %		91.5	95.2	92.6	90.9
<i>F</i> (000)		260	1328	1368	514
Refined parameters		151	177	178	289
Goodness-of-fit on <i>F</i> ² (<i>S</i>) ^a		1.047	0.952	1.137	1.578
Final <i>R</i> _{<i>i</i>} ^b factor [<i>I</i> > 2 σ (<i>I</i>)]		0.0698	0.0812	0.0411	0.1226
<i>wR</i> ₂ ^c factor (all data)		0.2089	0.2415	0.1131	0.3939
Largest diff. peak/hole / (e Å ⁻³)		0.630/-0.526	1.931/-0.951	0.589/-0.539	1.857/-2.067
CCDC deposit No.		1869708	1869709	1869710	1869711

ρ_{calc} : calculated density; *F*(000): structure factor in the zeroth-order case; *F*²: squared structure factor; *wR*₂: *R*-value for *F*²; CCDC: Cambridge Crystallographic Data Centre.

Results and Discussion

Synthesis and characterization

The Na₂Hpcpa salt was used as water soluble source of the oxamate ligand, the complexation reaction being done by slow diffusion in H-shape tubes in order to grow X-ray quality crystals. The metal sources were iron(III) chloride, manganese(II) chloride and zinc(II) chloride for **1**, **2** and **3** respectively, whereas the [Cu(NO₃)(bipy)(H₂O)₃] NO₃ complex was used for **4**. Interestingly, a reduction of

the iron(III) to iron(II) occurs leading to the mononuclear compound of formula [Fe(H₂pcpa)₂(H₂O)₂] (**1**). The slow hydrolytic reaction of the oxamate (or the related oxamidate) to yield oxalate that has been observed by different authors either under ambient,^{20,57-61} or hydrothermal conditions⁶² is at the origin of this surprising result. This process is most likely accompanied by the well-known photo-induced ligand to metal charge transfer (LMCT) reaction of the iron(III)-oxalate to give rise to the (photo) generation of iron(II) ions⁶³⁻⁶⁵ which in turn can interact with the remaining oxamate. Also the hydrolysis of the iron(III) in

Table 2. Main bond lengths and angles for **1-4**^{a-c}

	Bond length / Å		Bond angle / degree			
1	Fe1–O4	2.141(3)	O4–Fe1–O4 ⁱ	180	O4 ⁱ –Fe1–O1W ⁱ	90.92(16)
	Fe1–O5	2.110(4)	O4–Fe1–O5	77.77(14)	O5–Fe1–O5 ⁱ	180.0
	Fe1–O1W	2.080(4)	O4–Fe1–O5 ⁱ	102.23(14)	O5–Fe1–O1W	90.91(18)
			O4–Fe1–O1W	90.92(16)	O5–Fe1–O1W ⁱ	89.09(18)
			O4–Fe1–O1W ⁱ	89.08(16)	O5 ⁱ –Fe1–O1W	89.09(18)
			O4 ⁱ –Fe1–O5	102.23(14)	O5 ⁱ –Fe1–O1W ⁱ	90.91(18)
			O4 ⁱ –Fe1–O5 ⁱ	77.77(14)	O1W–Fe1–O1W ⁱ	180.0
			O4 ⁱ –Fe1–O1W	89.08(16)		
2	Mn1–O1	2.045(5)	O1–Mn1–O4 ⁱ	90.72(19)	O4 ⁱ –Mn1–O3W	88.76(19)
	Mn1–O4 ⁱ	2.209(4)	O1–Mn1–O5 ⁱ	160.3(2)	O5 ⁱ –Mn1–O1W	96.09(17)
	Mn1–O5 ⁱ	2.210(5)	O1–Mn1–O1W	99.9(2)	O5 ⁱ –Mn1–O2W	84.40(18)
	Mn1–O1W	2.164(4)	O1–Mn1–O2W	84.7(2)	O5 ⁱ –Mn1–O3W	95.43(18)
	Mn1–O2W	2.234(5)	O1–Mn1–O3W	95.5(2)	O1W–Mn1–O2W	88.23(18)
	Mn1–O3W	2.217(5)	O4 ⁱ –Mn1–O5 ⁱ	73.18(16)	O1W–Mn1–O3W	91.72(18)
			O4 ⁱ –Mn1–O1W	169.25(17)	O2W–Mn1–O3W	179.81(19)
		O4 ⁱ –Mn1–O2W	91.25(19)			
3	Zn1–O1	1.980(3)	O1–Zn1–O4 ⁱ	88.97(11)	O4 ⁱ –Zn1–O3W	89.73(11)
	Zn1–O4 ⁱ	2.133(3)	O1–Zn1–O5 ⁱ	161.42(11)	O5 ⁱ –Zn1–O1W	93.42(10)
	Zn1–O5 ⁱ	2.133(3)	O1–Zn1–O1W	100.91(11)	O5 ⁱ –Zn1–O2W	84.97(10)
	Zn1–O1W	2.070(2)	O1–Zn1–O2W	83.95(11)	O5 ⁱ –Zn1–O3W	94.43(10)
	Zn1–O2W	2.179(3)	O1–Zn1–O3W	96.79(11)	O1W–Zn1–O2W	87.35(10)
	Zn1–O3W	2.129(3)	O4 ⁱ –Zn1–O5 ⁱ	76.30(9)	O1W–Zn1–O3W	92.04(10)
			O4 ⁱ –Zn1–O1W	169.68(10)	O2W–Zn1–O3W	179.12(9)
		O4 ⁱ –Zn1–O2W	90.76(10)			
4	Cu1–O1 ⁱ	2.255(6)	O1 ⁱ –Cu1–O4	94.2(2)	O4–Cu1–N2	94.1(3)
	Cu1–O4	2.005(7)	O1 ⁱ –Cu1–O5	92.7(3)	O4–Cu1–N3	163.8(3)
	Cu1–O5	1.931(7)	O1 ⁱ –Cu1–N2	99.3(3)	O5–Cu1–N2	167.9(3)
	Cu1–N2	1.965(9)	O1 ⁱ –Cu1–N3	102.0(3)	O5–Cu1–N3	96.8(3)
	Cu1–N3	1.953(9)	O4–Cu1–O5	83.9(3)	N2–Cu1–N3	81.8(3)

^aSymmetry code for **1**: (i) = 1 – x, –y, 1 – z; ^bsymmetry code for **2** and **3**: (i) = ½ + x, ½ – y, 1 – z; ^csymmetry code for **4**: (i) = 2 – x, 1 – y, 2 – z.

the aqueous solution would account for the presence of the H₂pcca[–] ligand in **1** instead of the initial monoprotonated Hpcca[–] form. These features are in agreement with the low yield of **1** (ca. 24%). In the case of zinc(II) and Mn^{II}, chains of formula {[Mn(Hpcca)(H₂O)₃]·1/2H₂O}_n (**2**) and {[Zn(Hpcca)(H₂O)₃]·1/2H₂O}_n (**3**) are obtained where the initial monoprotonated Hpcca[–] species is present adopting a bidentate/monodentate bridging mode (see below). Finally, as far as the copper(II) ion is concerned, the presence of the bidentate bipy ligand precludes the chain formation, the neutral dicopper(II) compound [Cu₂(Hpcca)₂(bipy)₂]·8H₂O (**4**) being formed, the Hpcca[–] ligand exhibiting the same coordination mode than in **2** and **3**.

In order to confirm the phase purity of the synthesized

compounds, their powder X-ray diffraction (PXRD) patterns were recorded. As shown in Figures S5–S8 (SI section), the PXRD patterns recorded for polycrystalline samples of **1–3** are in agreement with those simulated from the respective single-crystal X-ray data using the Mercury 2.4 program⁵⁴ demonstrating that the crystal structure is truly representative of the bulk materials. Based on the comparison between the experimental and simulated PXRD patterns of compound **4** (Figure S8, SI section), it is possible to find in the synthetic batch its crystal phase determined by single-crystal X-ray diffraction technique. However, a mixture of phases is present since there are several Bragg reflections which are not predicted from the corresponding crystal structure.

Broad absorption bands are observed in the diffuse electronic spectra of **1-4**. Intraligand $n\text{-}\pi^*$ and $\pi\text{-}\pi^*$ charge-transfer transitions (CT) occur below 400 nm (25000 cm^{-1}). The d-d transitions are observed at 442 nm for Fe^{II} shows distorted an octahedral geometry in **1** and at 690 nm for Cu^{II} shows a square pyramidal surrounding in **4**. A very weak spin-forbidden absorption which is observed for **2** at 540 nm is assigned to a d-d transition for Mn^{II} in a distorted octahedral geometry.

The IR spectra of **1-4** (Figures S1-S4, SI section) show strong and broad absorptions in the high frequency region (centered at ca. 3400 cm^{-1}) which are due to O–H stretching vibration of the water molecules together with the $\nu(\text{N-H})$ stretching vibrations of the amide fragment in H_2pcpa^- (**1**) and Hpcpa^{2-} (**2-4**) ligands, all of them involved in an extensive network of hydrogen bonds.⁶⁶ A sharp peak at 3360 cm^{-1} is the diagnostic of the presence of the amide N–H function in **1**, this absorption being masked by the O–H stretching vibrations in the other three complexes. Strong peaks in the range 1690-1600 cm^{-1} in the infrared spectra of **1-4** are due to $\nu_{\text{as}}(\text{COO}^-)$ and $\nu_{\text{as}}(\text{C=O})$ vibrations of the carboxylate and amide groups. The $(\delta(\text{C-H}_{\text{arom}}))$ deformation vibration of the phenyl ring of the *N*-substituted oxamate appears in the frequency range 790-770 cm^{-1} in the infrared spectra of **1-4**; an additional medium intensity peak at 731 cm^{-1} ($\delta(\text{C-H}_{\text{arom}})$) in the case of **4** is indicative of the presence of bipy in this compound. All these spectroscopic features in **1-4** have been confirmed by the X-ray structures (see below).

Description of the structures

[Fe(H_2pcpa)₂(H_2O)₂] (**1**)

The structure of compound **1** was solved in the P-1 space group and it consists of centrosymmetric mononuclear iron(II) units with two *trans*-positioned water molecules (O1W and O1Wⁱ) and two bidentate

monodeprotonate *N*-4-(carboxyphenyl)oxamate ligands (O4, O5, O4ⁱ and O5ⁱ) building a somewhat distorted octahedral surrounding (Figure 2). The root mean square deviation (r.m.s.d.) for the least squares (l.s.) basal plane defined by the four oxamate-oxygens did not show any significant error. An axial compression together with a significant rhombicity at the equatorial plane occurs around the iron atom, the value of the Fe–O_{water} bond distances (Fe1–O1W = Fe–O1Wⁱ = 2.080(4) Å) being shorter than the Fe–O_{oxamate} bond lengths (2.110(4) Å and 2.141(3) Å for Fe1–O5 and Fe1–O4, respectively). The reduced bite of the bidentate monoprotonated oxamate fragment (77.77(14)° for O4–Fe–O5) is one of the main sources for this distortion. Bond angles fall in the range 77.77(14)-102.23(14)° (see Table 2).

The neutral units of **1** are arranged in supramolecular zigzag chains parallel to crystallographic *c* axis which are in turn interlinked through hydrogen bonds along the *b* axis to result into a layered structure extending in the *bc* plane (Figure 3a, Table S1, SI section). These supramolecular layers are stacked along the [100] direction (Figure 3b). The presence of the carboxylic substituent at the phenyl ring precludes the expansion of the mononuclear unit as a coordination polymer (as occurs in **2** and **3**, see below). One can see how the molecular packing of **1** is built-up by intermolecular hydrogen bonds between pairs of carboxylic groups along the crystallographic *c* axis though the formation of R₂²(6) synthon together with a bifurcated hydrogen bond involving the coordinated water molecule (O1Wⁱⁱ) of one complex unit and the carboxylate-monodeprotonated oxamate-oxygen atoms (O3 and O5) of an adjacent entity along the crystallographic *b* axis.

The values of the shortest intralayer iron-iron separation are 5.9688(7) Å (Fe1ⁱⁱ⋯Fe1ⁱⁱⁱ) and 21.096(1) Å (Fe1ⁱⁱⁱ⋯Fe1ⁱⁱⁱⁱ) whereas that of shortest the interlayer metal-metal distance is 4.8094(4) Å (Fe1ⁱⁱⁱ⋯Fe1^{iv}).

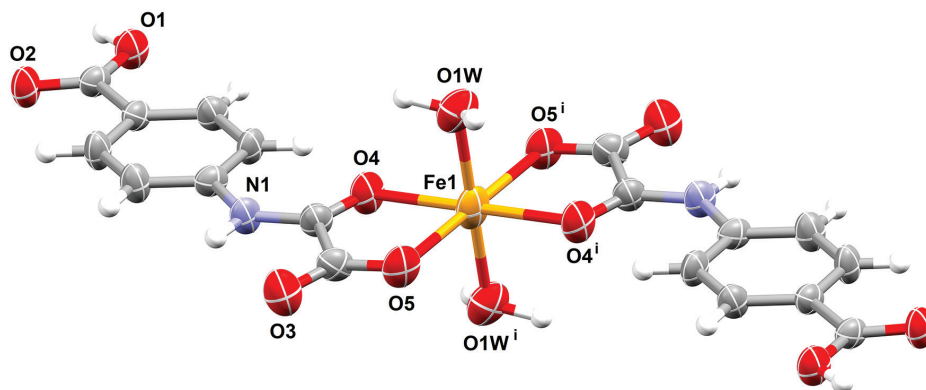


Figure 2. Drawing of the structure of **1** with the thermal ellipsoids of the non-hydrogen atoms at the 50% probability level. The labels of hydrogen and carbon atoms were omitted for clarity (symmetry code: (i) = 1 – x, –y, 1 – z).

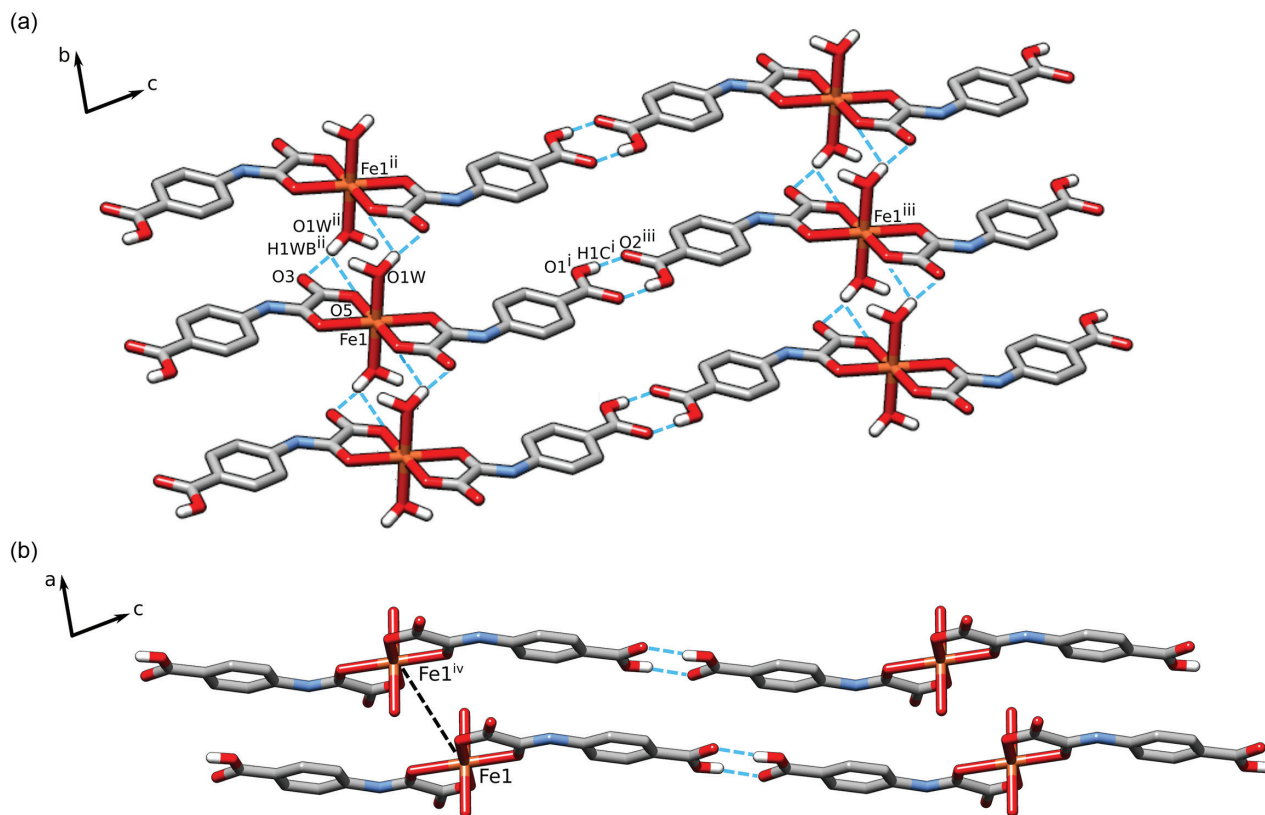


Figure 3. (a) View of a fragment of the supramolecular layer of **1** extending in the crystallographic *bc* plane. The hydrogen bonds are represented as dashed cyan lines. (b) View of the stacking of the supramolecular layers along the [100] direction (symmetry codes: (ii) = $x, 1 + y, z$; (iii) = $2 + x, y, 1 + z$; (iv) = $1 + x, y, z$).

$\{[\text{Mn}(\text{Hpcpa})(\text{H}_2\text{O})_3] \cdot 1/2\text{H}_2\text{O}\}_n$ (**2**) and $\{[\text{Zn}(\text{Hpcpa})(\text{H}_2\text{O})_3] \cdot 1/2\text{H}_2\text{O}\}_n$ (**3**)

Compounds **2** and **3** are isostructural and their structure was solved in the *Pbcn* space group. One manganese(II) (**2**)/zinc(II) (**3**) a Hpcpa^{2-} anion and three coordinated (O1W , O2W and O3W) and a free (O4W) water molecules constitute the asymmetric unit (Figure 4). The water oxygen O4W is located on a glide plane and therefore is only half occupied. Each Hpcpa^{2-} ligand in **2** and **3** adopts a monodentate/bidentate bridging through a carboxylate-oxygen (O1) of a monodeprotonated oxamate fragment and two *cis* oxygen atoms (O4^i and O5^i) from another

symmetry-related Hpcpa^{2-} ligand towards the metal center [Mn1 (**2**) and Zn1 (**3**)] the whole leading to neutral zigzag chains running parallel to the crystallographic *a* axis (see Figure 5).

Each crystallographically independent metal atom in **2** and **3** is six-coordinate in a somewhat distorted octahedral surrounding built by three *mer* positioned water molecules (O1W , O2W and O3W) and three oxygen atoms (O1 , O4^i and O5^i) from two Hpcpa^{2-} ligands. The r.m.s.d. for the l.s. planes were 0.202 and 0.170 Å in **2** and **3**, respectively. The $\text{O1O4}^i\text{O5}^i\text{O1W}$ set of atoms define the basal plane and the O2W and O3W water molecules fill the axial positions around

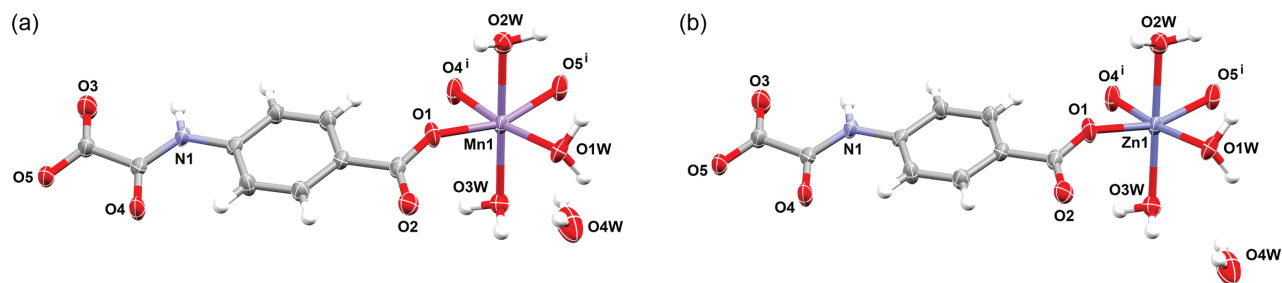


Figure 4. Asymmetric unit of (a) **2** and (b) **3** with thermal ellipsoids of the non-hydrogen atoms at the 50% probability level. The labels of hydrogen and carbon atoms were omitted for clarity (symmetry code: (i) = $1/2 + x, 1/2 - y, 1 - z$).

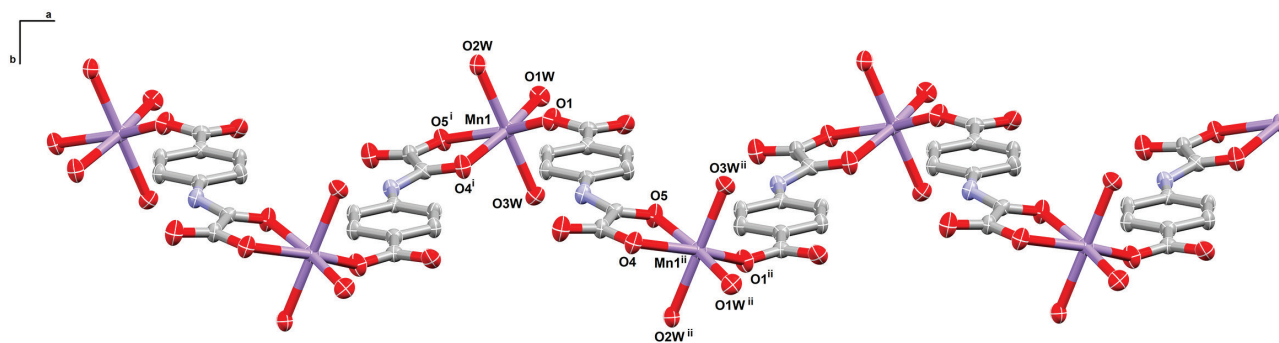


Figure 5. View of a fragment of the neutral zigzag chain of **2** running parallel to the crystallographic *a* axis (the same drawing is done for **3**; see Figure S9, SI section) (symmetry code: (ii) = $-\frac{1}{2} + x, \frac{1}{2} - y, 1 - z$).

the metal centers. The largest deviated atom from these planes is O4 for both structures, with distances of 0.120(2) Å (**2**) and 0.094(17) Å (**3**). The metal atom is away from the l.s. plane by 0.107(1) Å (**1**) and 0.120(5) Å (**2**). The values of the M–O_w and M–O_{hpcpa} cover the ranges 2.164(4)–2.234(5) Å and 2.045(5)–2.210(5) Å for **2** and 2.070(2)–2.179(3) Å and 1.980(3)–2.133(3) Å for **3** (see Table 2). As in **1**, the main source of the distortion of the octahedral surrounding at the metal atom in **2** and **3** is the reduced bite of the bidentate coordination of the monoprotonated oxamate ($O4^i-M-O5^i = 73.18(16)^\circ$ (**2**) and $76.30(9)^\circ$).

Given that **2** and **3** are isostructural compounds, their crystal packing is the same and then we will focus only on that of **2** and refer to the one of **3** for comparison. The neutral chains growing along the *a* axis are arranged by blocks in the crystallographic *ac* plane (Figure 6a) leading to a supramolecular layer where the neighboring chains are interlinked by hydrogen bonds along the *c* axis involving one the coordinated water molecule (O1W) and one carboxylate-oxygen (O5) ($O1W \cdots O5^{iii} = 2.697(6)$ Å;

symmetry code: (iii) = $-x, y, 3/2 + z$) from the coordinated monoprotonated oxamate of an adjacent chain (Figure 6b). Additional hydrogen bonds and π - π stacking interactions occur along the crystallographic *b* axis in **2** and **3** (Figure 7) that lead to a supramolecular three-dimensional network. The values of the distance between the centroids in the π - π stacking, calculated through the atoms of aromatic ring labeled C2–C7, is 3.669(10) Å (**2**) and 3.639(19) Å (**3**). Details of the hydrogen bonding pattern for **2** and **3** are listed in Table S1, SI section.

The values of the metal-metal distance across the bridging Hpcpa²⁻ ligand are 11.46(10) Å (Mn1 \cdots Mn1ⁱⁱ) and 11.326(8) Å (Zn1 \cdots Zn1ⁱⁱ), whereas the shortest interchain metal-metal separation are 5.1449(12) Å (Mn1 \cdots Mn1ⁱⁱⁱ), 5.8195(14) Å (Mn1 \cdots Mn1^{vii}), 5.0961(8) Å (Zn1 \cdots Zn1ⁱⁱⁱ) and 5.7423(7) Å (Zn1 \cdots Zn1^{viii}).

[Cu₂(Hpcpa)₂(bipy)₂]·8H₂O (**4**)

The structure of **4** was solved in the P-1 space group and its structure consists of centrosymmetric dicopper(II)

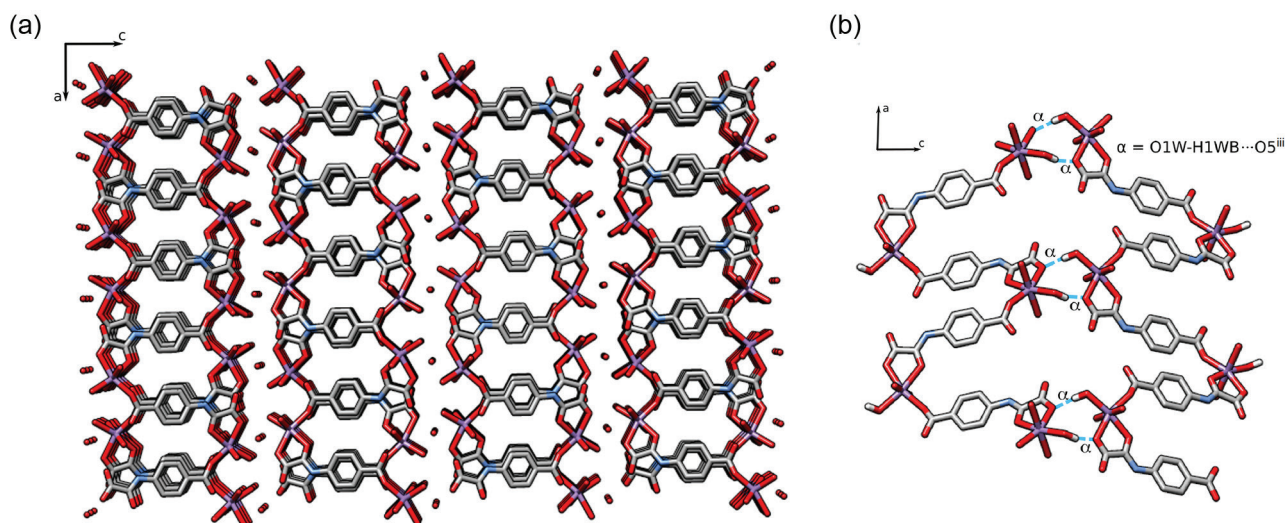


Figure 6. (a) A view of the crystal packing of **2** showing the arrangement of the chains in the crystallographic *ac* plane. (b) A detail of the hydrogen bonds (dashed blue lines) linking adjacent chains of **2** in the *ac* plane.

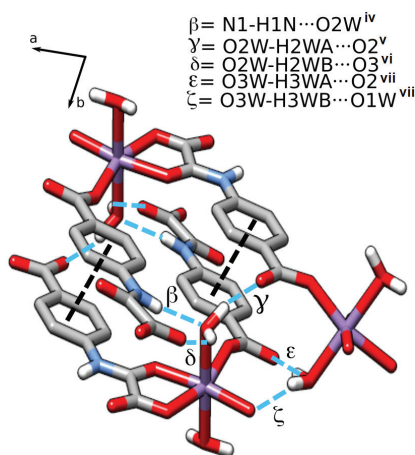


Figure 7. Intermolecular interactions in **2** along the crystallographic *b* axis through hydrogen bonds (dashed blue lines) and π - π stacking (dashed black lines) (symmetry code: (iv) = $\frac{1}{2} - x, -\frac{1}{2} - y, z$; (v) = $\frac{1}{2} - x, -\frac{1}{2} + y, z$; (vi) = $-x, -y, 1 - z$; (vii) = $\frac{1}{2} - x, \frac{1}{2} + y, z$).

units of formula $[\text{Cu}_2(\text{Hpcpa})_2(\text{bipy})_2]$ and water molecules of crystallization. A view of the asymmetric unit is shown in Figure 8a. The Hpcpa²⁻ ligand in **4** adopts the bidentate/monodentate coordination mode as in **2** and **3** but the presence of the bipy acting as an end-cap chelating ligand precludes the formation of a chain in **4** in contrast to what occurs in **2** and **3** (Figure 8b).

Each copper(II) ion in **4** is five-coordinate in a distorted square pyramidal surrounding with two nitrogen atoms of a chelating bipy (N2 and N3) plus two oxygen atoms (O4 and O5) from a bidentate monoprotonated oxamate of a Hpcpa²⁻ ligand building the basal plane and a carboxylate-oxygen (O1ⁱ) from a symmetry related Hpcpa²⁻ ligand at the apical position. The value of trigonality parameter (τ) is equal to 0.069 ($\tau = 0$ and 1 for ideal square-pyramidal and trigonal-bipyramidal, respectively).⁶⁷ The root mean square deviation for the least-squares plane defined by the N2N3O4O5 set of atoms is 0.071 Å. The greatest deviated atoms from this l.s. plane were N2 and N3, both of them

with a deviation of 0.043(7) Å, while Cu²⁺ is shifted from this l.s. plane by 0.2402(11) Å. The basal Cu–O_{carboxylate} bond length (Cu1–O5 = 1.931(7) Å) is shorter than the Cu–O_{amide-oxygen} (Cu1–O4 = 2.005(7) Å) as expected because of the greater basicity of the carboxylate oxygen *versus* the amide-oxygen, both bond lengths being shorter than the axial copper-to-oxygen interaction (Cu1–O1ⁱ = 2.255(6) Å). The values of the angles subtended at the copper(II) ion by the chelating bipy and monoprotonated oxamate fragment are 81.8(3) and 83.9(3)°, respectively.

The crystal packing is constituted by layers of neutral dicopper(II) units which are arranged parallel to *ac* plane, the dimers being oriented in [101] direction, with non-coordinated water molecules in their surrounding (see Figure 9).

The intermolecular interactions connecting the dicopper(II) occur along the three crystallographic axes, being mainly cross-linked by water molecules (see Table S1, SI section). However, hydrogen bonds are not the only relevant interaction between the dicopper(II) entities. The π - π interactions along the crystallographic *a* axis also contribute to the stabilization of the crystal structure. There are two π - π type interactions between the dinuclear units, one involving the centroids defined as Cg1 and Cg2 and another one engaging Cg2 and Cg3. These centroids were fitted through atoms of the phenyl ring from the Hpcpa²⁻ and each pyridyl ring from the bipy molecule, respectively. The distance between those centroids are 3.767(5) and 3.722(5) Å in the two interactions, respectively. All these interactions are shown in Figure 10.

The intramolecular copper-copper separation is 9.975(2) Å (Cu1ⁱ–Cu1ⁱ) whereas the shortest intermolecular copper-copper distances are 6.0561(19) and 7.385(2) Å for Cuⁱ–Cuⁱⁱ and Cuⁱ–Cuⁱⁱⁱ, respectively, (symmetry code: (ii) = $1 - x, 1 - y, 2 - z$; (iii) = $1 - x, 1 - y, 1 - z$). These two last values correspond to π - π stacking between dicopper(II)

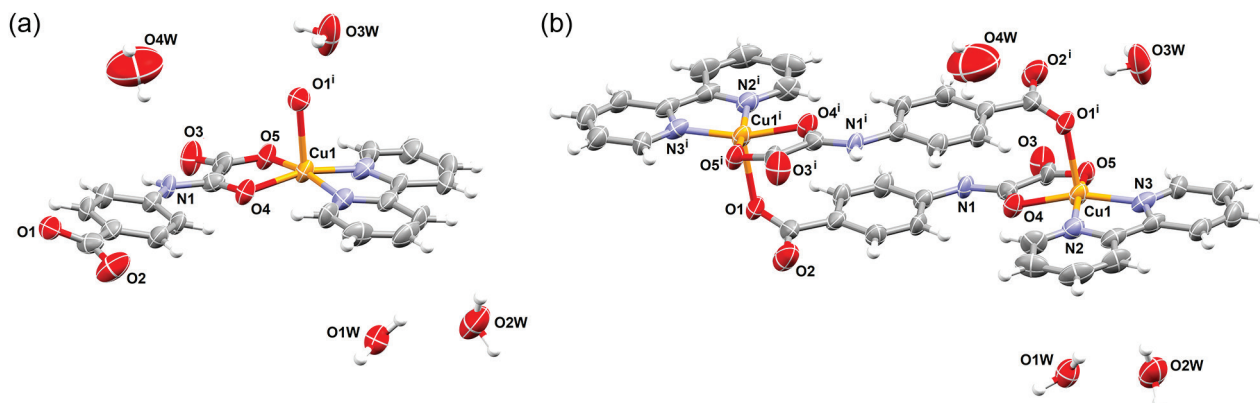


Figure 8. (a) Asymmetric unit of **4** with thermal ellipsoids of the non-hydrogen atoms at the 50% probability level. The labels of hydrogen and carbon atoms were omitted for clarity. (b) Perspective drawing of the dicopper(II) unit of **4**. Symmetry code: (i) = $2 - x, 1 - y, 2 - z$.

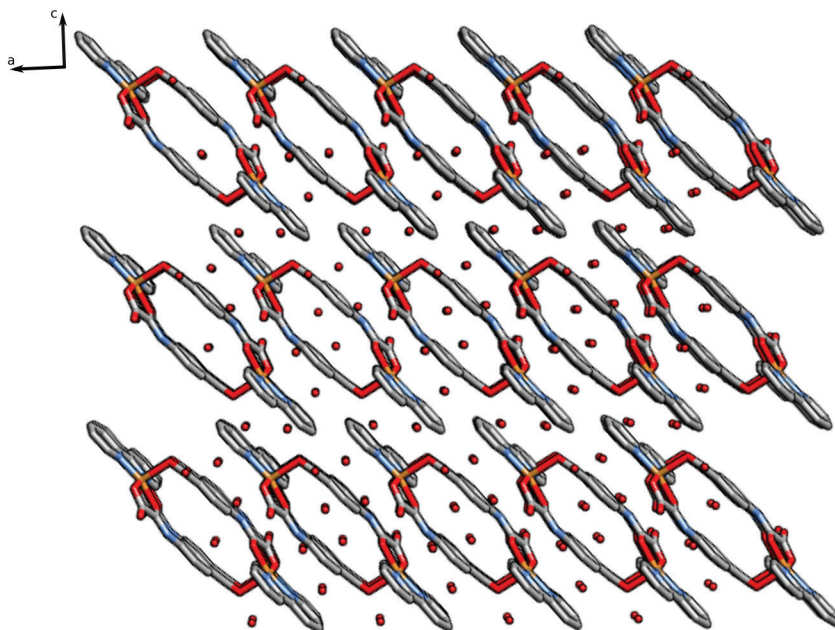


Figure 9. View of the crystal packing of **4** showing the layered arrangement of the dicopper(II) units parallel to the crystallographic *ac* plane together with the water molecules of crystallization.

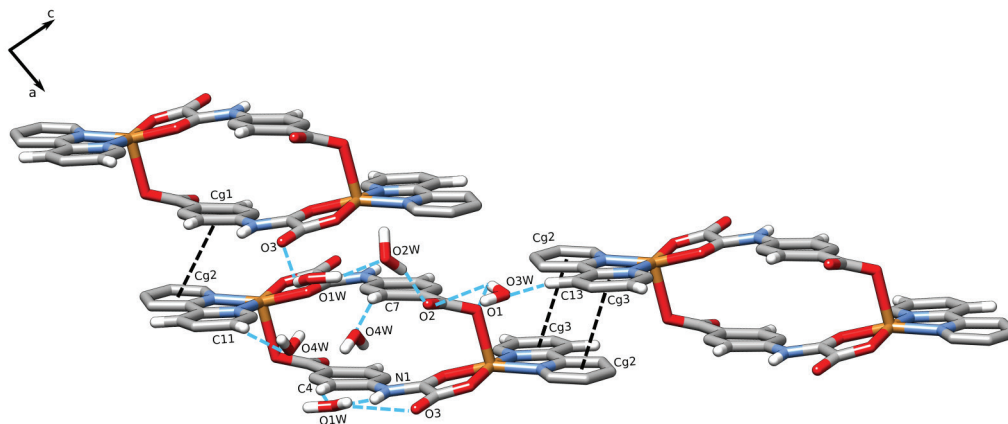


Figure 10. Intermolecular interactions between three dicopper(II) units, connected by hydrogen bonds (dashed cyan lines) along the crystallographic *a* and *c* axes and π - π stacking (dashed black line) along the *a* axis.

units, whose distances are measured between the metal atoms from dimers interacting through Cg1–Cg2 and Cg2–Cg3, respectively.

The coordination of transition metal ions to nitrogen from pyridines (1,10-phenanthroline and bipy) concomitantly to oxamate ligands are already known.^{68–70} Unlike to the present structure, complexes bearing bipy contain also two oxamate bridges.⁶⁸ These last ligands allowed the formation of discrete (including one dimer) and coordination polymers. On the other hand, the structure of **4** reported herein reveals the occurrence of an isolated dicopper(II) complex, although it shows only one oxamate bridge and one deprotonated carboxylic acid acting as ligands. The dimer from literature⁶⁹ shows a closer distance between metals ions than that found here, which is justified by the

stacking of one pyridyl ring on the top of an oxamate bridge from different coordination compounds. Nevertheless, the structure of **4** represents the first report with carboxylate, oxamate and bipy groups coordinated to the metal center. Among all other structures with only the Hpcpa²⁻ ligand, which were reported by some of us, it was also verified the formation of both a coordination polymer and a dimer, indicating the versatility of the Hpcpa²⁻ ligand to output complexes with different dimensionality.³⁹

Crystal structures of coordination compound with carboxylic acid allied to an oxamate bridge as ligands are limited in the literature. Analyzing the Cambridge Structural Database (CSD version 5.39, May 2018),⁷¹ only three coordination compounds with those features were found.^{39,72} Among these, two of them were reported

by our research group, which show the MeHpcpa⁻ and Hpcpa²⁻ ligands (CCDC refcode: VOPLIX and VOQDEM, respectively).³⁹ The other one contains two oxamate bridges and only one deprotonated carboxylic acid, which changed therefore the geometry of the final complex and led to an entirely different packing due to a further coordination to an alkaline metal.⁷² Moreover, all these three structures contain the protonated carboxylic acid, as observed in **1**. The presence of this acid hydrogen limited the formation of a coordination polymer, which results in an isolated coordination compound, as mentioned. Meanwhile, structures **2** and **3** are isostructural between each other and to VOQDEM,³⁹ which has the formula $\{[\text{Co}(\text{Hpcpa})(\text{H}_2\text{O})_3] \cdot 1/2\text{H}_2\text{O}\}_n$.

Magnetic properties

For pedagogical reasons, we will focus first on the magnetic properties of **4** followed by those of **2** and finally, we will present those of **1** (compound **3** being a diamagnetic species).

The magnetic properties of **4** under the form of $\chi_M T$ versus T plot (χ_M is the magnetic susceptibility *per* dicopper(II) unit) are shown in Figure 11. $\chi_M T$ at room temperature is equal to 0.827 cm³ mol⁻¹ K, a value which is as expected for two magnetically isolated spin doublets. Upon cooling down, this value remains constant until ca. 50 K and it further decreases to 0.766 cm³ mol⁻¹ K at 1.9 K. This small decrease at low temperatures is due to a weak antiferromagnetic interaction between the copper(II) ions. Following the dinuclear structure of **4**, its magnetic data were analyzed through equation 1.⁷³

$$\chi_M = (2N\beta^2 g^2 / kT) [3 + \exp(-J/kT)]^{-1} \quad (1)$$

which is the Bleaney-Bowers expression for a coupled dinuclear system with local spin doublets, the spin Hamiltonian being defined as $\mathbf{H} = -J\mathbf{S}_{\text{Cu}^1} \cdot \mathbf{S}_{\text{Cu}^2} + \beta\mathbf{H}(g_{\text{Cu}^1}\mathbf{S}_{\text{Cu}^1} + g_{\text{Cu}^2}\mathbf{S}_{\text{Cu}^2})$, where N is Avogadro's number, β is the Bohr magneton, g is the splitting factor, J is exchange coupling constant and \mathbf{S} is spin values, $S_{\text{Cu}^1} = S_{\text{Cu}^2} = 1/2$ and $g = g_{\text{Cu}^1} = g_{\text{Cu}^2}$. Least-squares best-fit parameters for **4** are $J = -0.390(2)$ cm⁻¹ and $g = 2.101(5)$ with $R = 2.1 \times 10^{-6}$ (R is the agreement factor defined as $\sum_i [(\chi_M T)_{\text{obs}}(i) - (\chi_M T)_{\text{calc}}(i)]^2 / \sum_i [(\chi_M T)_{\text{obs}}(i)]^2$).

This very small value of J found for this compound can be understood by looking at the relative disposition of the magnetic orbitals involved and the large intramolecular copper-copper separation. In fact, the magnetic orbital at each copper(II) site (that is the molecular orbital that describes its unpaired electron) is of the $d(x^2-y^2)$ -type and it is mainly delocalized on the equatorial plane, the spin density

on the apical position (O1ⁱ atom) is predicted to be very small. The overlap between the parallel $d(x^2-y^2)$ magnetic orbitals through the extended Hpcpa⁻ bridge connecting an equatorial position at one copper center with the apical site at the other one, the copper-copper separation being ca. 9.98 Å (Cuⁱ...Cuⁱ), is expected to be very small, if any. The poor overlap between these magnetic orbitals across the multiatom Hpcpa⁻ bridge would account for the weak antiferromagnetic coupling observed its magnitude being proportional to the square of overlap integral after the Kahn's model.^{74,75} Anyway, this value of J in **4** has to be considered as the upper limit given that there are intermolecular copper-copper distances which are shorter than the intramolecular ones through π - π stacking (6.0561(19) and 7.385(2) Å for Cuⁱ...Cuⁱⁱ and Cuⁱ...Cuⁱⁱⁱ, respectively).

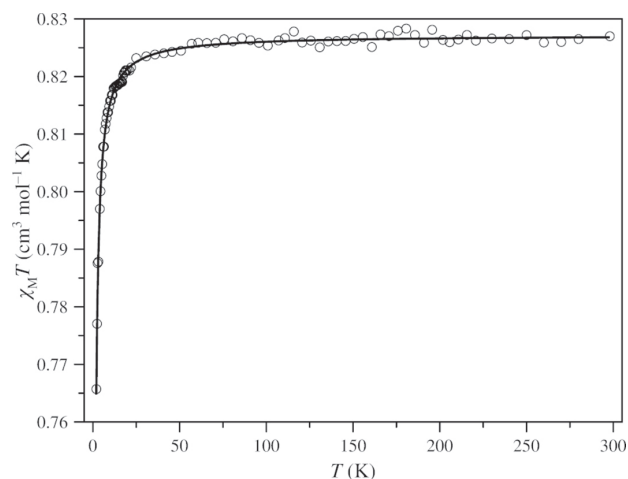


Figure 11. Temperature dependence of $\chi_M T$ for **4**: (o) experimental; (—) best-fit curve through equation 1 (see text).

The magnetic properties of **2** under the form of $\chi_M T$ versus T plot (χ_M is the magnetic susceptibility *per* two manganese(II) ions) are shown in Figure 12. $\chi_M T$ at room temperature is equal to 8.90 cm³ mol⁻¹ K, a value which is as expected for two magnetically isolated spin sextets. Upon cooling, this value remains constant until 60 K and it further decrease to 6.31 cm³ mol⁻¹ K at 1.9 K. The trend of this data is indicative of a weak antiferromagnetic interaction between the local spin sextets.

An inspection of the structure of **2** shows the presence of two possible exchange pathways: (i) the intrachain one, provided by the bidentate/monodentate Hpcpa²⁻ bridge with an intrachain metal-metal separation of 11.46(10) Å (Mnⁱ...Mnⁱⁱ) and (ii) the shorter interchain interactions of 5.1449(12) Å through O1W-H1WB...O5ⁱⁱ (Mnⁱ...Mnⁱⁱⁱ) and 5.8195(14) Å across O3W-H3W...O1W^{vii} (Mnⁱ...Mn^{vii}). Having in mind the much shorter interchain separation through the (ii) pathway, it is reasonable to discard the (i) one. Then, we analyzed the magnetic data of **2**

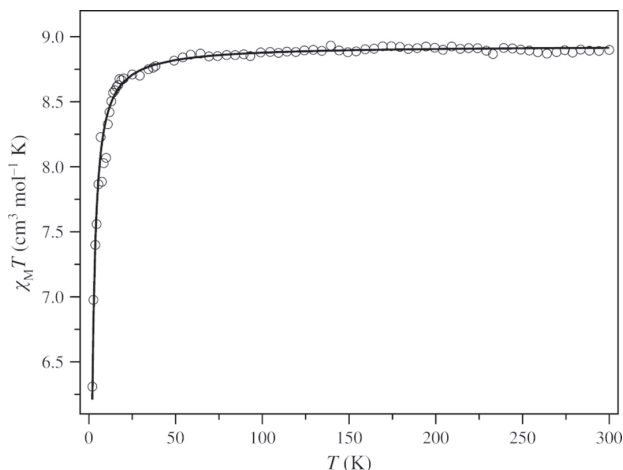


Figure 12. Temperature dependence of $\chi_M T$ for **2**: (o) experimental; (–) best-fit curve through equations 2-4 (see text).

through the expression for a discrete dimanganese(II) unit (equations 2-4).

$$\chi_M = (N\beta^2 g^2 / kT)[A/B] \quad (2)$$

with

$$A = \exp(x) + 5\exp(3x) + 14\exp(6x) + 30\exp(10x) + 55\exp(15x) \quad (3)$$

and

$$B = 1 + 3\exp(x) + 5\exp(3x) + 7\exp(6x) + 9\exp(10x) + 11\exp(15x) \quad (4)$$

where $x = J/k$, the spin Hamiltonian being defined as $H = -JS_{Mn1}S_{Mn2} + \beta H(g_{Mn1}S_{Mn1} + g_{Mn2}S_{Mn2})$. In the recent case, $S_{Mn1} = S_{Mn2} = 5/2$ and $g = g_{Mn1} = g_{Mn2}$. Least-squares best-fit parameters for **2** are $J = -0.221(1) \text{ cm}^{-1}$, $g = 2.020(5)$ and $R = 1.6 \times 10^{-5}$. The calculated curve matches well the experimental data in the whole temperature range explored.

Dealing with the weak antiferromagnetic coupling observed in **2**, previous magneto-structural studies have shown that hydrogen bonds are capable to be relatively good mediators of magnetic interactions.^{76,77} In this respect, values from weak ferro- to intermediate antiferromagnetic couplings were achieved in dicopper(II) complexes.⁷⁸ As far as we know, no data for magnetic coupling in a dinuclear manganese(II) species mediated by hydrogen bonds is available. A close case to **2** is a high-spin iron(III) compound ($S_{Fe} = 5/2$) of formula $[\text{Fe}(\text{bpym})\text{Cl}_3(\text{H}_2\text{O})]\cdot\text{H}_2\text{O}$ (bpym = 2,2'-bipyrimidine) where a value of J of -0.68 cm^{-1} was reported through the $\text{Fe}^{\text{III}}-\text{O}^{\text{W}}-\text{H}\cdots\text{Cl}-\text{Fe}^{\text{III}}$ exchange pathway.⁷⁹

The dc magnetic properties of **1** in the form of $\chi_M T$ against T plot (χ_M is the magnetic susceptibility per one iron(II) ion) are shown in Figure 13. $\chi_M T$ at room temperature is $3.64 \text{ cm}^3 \text{ mol}^{-1} \text{ K}$, a value which confirms the occurrence high-spin iron(II) ion ($S_{Fe} = 2$) with a g_{Fe} value largely above that for the free electron in this compound. Upon cooling, this value of $\chi_M T$ smoothly increases up to around 75 K, and it further decreases to $2.18 \text{ cm}^3 \text{ mol}^{-1} \text{ K}$ at 1.9 K. The trend in the high temperature range is due to the first-order SOC, whereas its subsequent decrease below 75 K could be attributed to either the SOC or zfs effects together with intermolecular antiferromagnetic interactions. An inspection of the crystal packing of **1** shows that occurrence of a supramolecular uniform iron(II) chain along the crystallographic c axis, the possible exchange pathway being provided by the bifurcated $\text{Fe}^{\text{II}}-\text{O}^{\text{I}}\text{W}^{\text{II}}-\text{H}^{\text{I}}\text{W}^{\text{II}}\cdots\text{O}^{\text{I}}-\text{C}^{\text{I}}-\text{O}^{\text{I}}-\text{Fe}^{\text{I}}$ hydrogen bond pathway (and its symmetry related), the iron-iron separation being ca. 6.0 \AA (see Figure 3a). In the light of this large metal-metal separation, we discard the occurrence of any significant intermolecular magnetic interaction.

Given that the magnetic properties of magnetically isolated six-coordinate iron(II) complexes are usually controlled by a first-order spin-orbit coupling (SOC), the use of the SOC Hamiltonian introduced through the T-P isomorphism constitutes an appropriate option to analyze their magnetic properties. The presence of a $^5T_{2g}$ ground state that does not mix with other ones supports the use of this approach. Therefore, the magnetic susceptibility of **1** were analyzed by means of the Hamiltonian of equation 5.

$$H = -\kappa\lambda L_{Fe} S_{Fe} + \Delta[L_{z,Fe} - L(L+1)/3] + \beta H(-\kappa L_{Fe} + g_e S_{Fe}) \quad (5)$$

In this Hamiltonian, λ is the spin-orbit coupling, κ accounts for the reduction of the orbital momentum (L) caused by the delocalization of the unpaired electrons and Δ is the energy gap between the $^5B_{2g}$ and 5E_g levels arising from the splitting of the $^5T_{2g}$ ground state through an axial distortion of the O_h symmetry. Best-fit parameters through the VPMAG package⁸⁰ in the temperature range 300-5 K are $\kappa = 0.935(2)$, $\lambda = -67.4(2) \text{ cm}^{-1}$, $\Delta = -383.6(4) \text{ cm}^{-1}$, and $R = 2.3 \times 10^{-5}$. The values of κ and λ show that there is an important covalent reduction, which is usual in complexes of the first-row transition metal ions. These values are in the range of those previously reported for mononuclear high-spin six-coordinate iron(II) complexes.⁸¹ On the other hand, the large Δ value agrees with the different electronic nature of the ligands occupying the axial and the equatorial positions of the six-coordinate environment.

As the orbital angular momentum in the ground state of the high-spin iron(II) complexes is not quenched by the ligand field, the resulting strong “in state” SOC can lead to a sizable axial zero-field splitting (zfs) parameter D .⁸² In fact, the large Δ value supports a strong splitting of the ${}^5T_{2g}$ ground state into the ${}^5B_{2g}$ and 5E_g levels. Moreover, the different nature of the donor atoms in the equatorial plane at the metal center allows to describe a rhombic distortion through two different directions arising from the *trans* arrangement of the monoprotonated oxamate fragment, which leads to a splitting of the low-lying 5E_g level. Being this splitting large enough, the three states coming from the ${}^5T_{2g}$ ground state are well separated and do not present any orbital momentum. Having this in mind, a zfs approach should be also appropriated. So, CASSCF/NEVPT2 calculations reveal that the energies of the two excited levels are 1097 and 2239 cm^{-1} above the ground level. The phenomenological approach based on the zfs used to analyze the magnetic susceptibility of **1** is summarized in the Hamiltonian of equation 6.

$$H_{zfs+Zeeman} = D[S_z^2 - S(S+1)] + \beta H_g S \quad (6)$$

The best-fit parameters through the VPMAG package⁸⁰ in the temperature range 300-5 K are $D = -11.7(2) \text{ cm}^{-1}$, $g = 2.296(3)$, temperature-independent paramagnetism (TIP) = $-1040(40) \times 10^{-6} \text{ cm}^3 \text{ mol}^{-1}$ and $R = 3.1 \times 10^{-5}$. In this approach where 1st order SOC can be present, the temperature-independent paramagnetism accounts for the depopulation at high temperatures of the closest excited states. The negative sign for the D parameter has its origin in the axial compression as indicated by the negative value of the Δ parameter. The fact that the $\chi_M T$ at very low temperatures do not tend to vanish, also supports a negative value for D . Moreover, this is confirmed by *ab initio* CASSCF/NEVPT2 calculations on the real geometry of **1** which conducted through the version 4.0 of the ORCA programme,⁴⁵ afforded negative axial and non-negligible transverse zfs parameters: $D = -10.1 \text{ cm}^{-1}$ and $E/|D| = 0.126 \text{ cm}^{-1}$. Interestingly, the negative value of D , together with its relative large size, indicates an intrinsic spin-reversal energy barrier of $U_{\text{eff}} = S^2|D| = 40.4 \text{ cm}^{-1}$, and consequently the possibility of slow magnetic relaxation. Also the negative value of D value for **1** confirms its uniaxial anisotropy and its magnitude is comparable with those of other two-,⁸³ three-,⁸⁴ four-,^{84,85-87} six-,^{88,89} seven-^{90,91} and eight-coordinate^{92,93} iron(II) complexes from the literature. As mentioned above, the rhombicity in **1** has its origin in the fact that the two bidentate monoprotonated oxamate ligands building the equatorial plane exhibit a *trans* arrangement. The origin of the axial anisotropy mainly

lies on the contributions from the low-lying quintet states ($D_Q = -8.8 \text{ cm}^{-1}$) although those from the triplet states are not completely negligible ($D_T = -1.3 \text{ cm}^{-1}$). Among the states that contribute to the D parameter, those arising from the ${}^5T_{2g}$ term are the dominant ones (see Table S2, SI section).

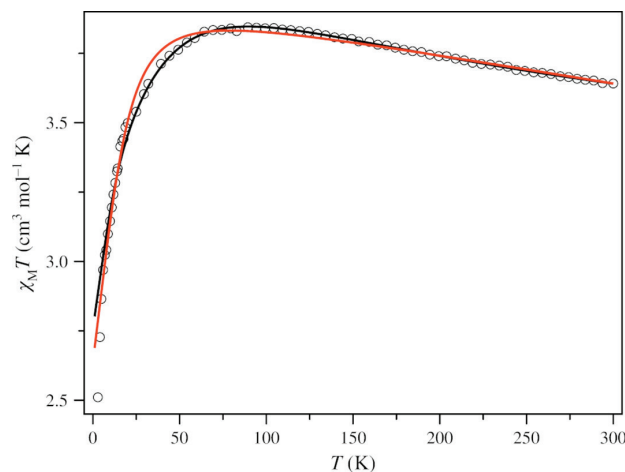


Figure 13. Temperature dependence of $\chi_M T$ for **1**: (o) experimental; (solid line) best-fit curve through SOC (black) and zfs (red) approaches (see text).

To probe the magnetization dynamics of **1**, alternating current (ac) magnetic susceptibility measurements have been carried out for this compound below 12 K. In the absence of an applied dc field, no χ_M'' signal was observed at frequencies up to 10000 Hz and temperatures down to 2.0 K. However, the application of external dc field (H_{dc}) of 5000 G (Figure 14) resulted in a set of frequency-dependent peaks in plots of χ_M'' versus T . These features suggest the occurrence of fast tunneling of the magnetization (QTM) that is removed under non-zero applied dc fields. Figure 14b shows the presence of more than one relaxation process, and χ_M'' shows well-defined peaks with the temperature only at a limited number of frequencies, being they incipient or hidden out-phase signals in most cases. This feature makes difficult the analysis of the dynamical behavior. In such cases, particularly in those where no peaks can be observed, there is an alternative to study the mechanisms that govern the slow relaxation of the magnetization.

In the past, the $\ln(\chi_M''/\chi_M')$ vs. $1/T$ plots have been useful in this kind of studies. Usually, these plots are limited to the range of temperature where just a relaxation process occurs, that is at high temperatures and above the temperature where χ_M'' shows a maximum. In such cases, the slope of the plots should be frequency independent. This approach usually works well although the reality is not so simple. Figure 15 show these plots for **1** in the whole temperature range. The curvature of these plots points out that several relaxation mechanisms are competing, and

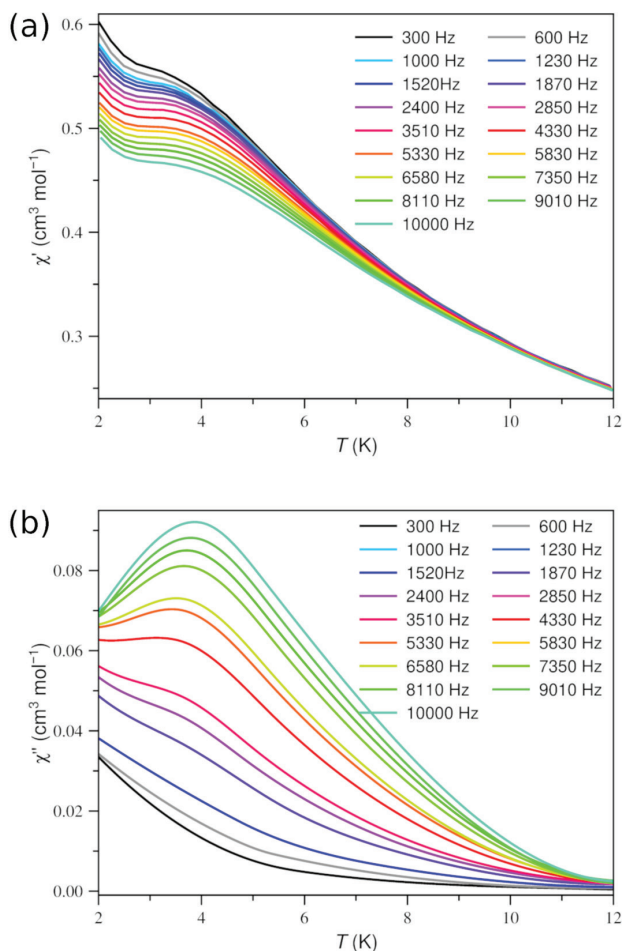


Figure 14. Frequency dependence of the in-phase (a) and out-of-phase (b) ac susceptibilities for **1** under an applied static field $H_{dc} = 5000$ G with a ± 5.0 G oscillating field at frequencies in the range 0.3-10 kHz.

they are linear just at high temperature. The $\ln(\chi_M''/\chi_M')$ remains constant at low temperatures, which is a signature of a predominant quantum-tunneling in this domain. In the light of these features, we will choose the model consisting of two Orbach processes to treat the high and intermediate temperature domains together with a quantum-tunneling describing the behavior at low temperatures (see equation 7).

$$\tau^{-1} = \tau_{01}^{-1} \exp(-E_{a1}) / kT + \tau_{02}^{-1} \exp(-E_{a2}) / kT + B \quad (7)$$

where E_{ai} and τ_{0i} are the activation energy and preexponential factor of the Orbach processes, and B is the quantum-tunneling term. The best-fit appears as bold lines in Figure 15, the obtained values of the parameters being the following: $E_{a1} = 43.2$ cm⁻¹, $\tau_{01} = 8.4 \times 10^{-8}$ s, $E_{a2} = 6.8$ cm⁻¹, $\tau_{02} = 2.0 \times 10^{-5}$ s and $B = 4960$ s⁻¹.

The most common is to consider two-phonon plus one-phonon competing relaxation processes. In this sense, we have replaced the second Orbach process showing a

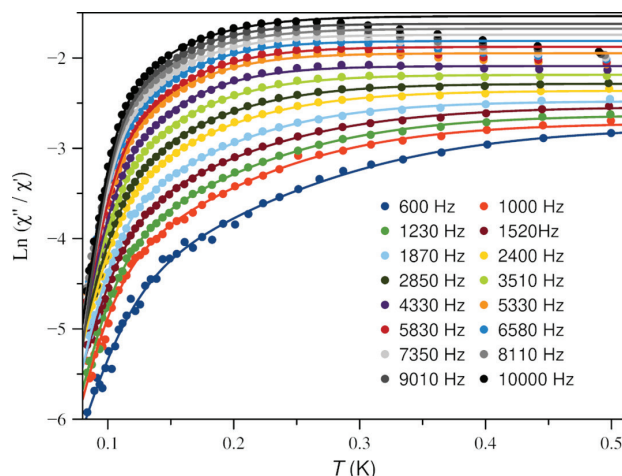


Figure 15. $\ln(\chi_M''/\chi_M')$ vs. $1/T$ plots for **1** under an applied static field $H_{dc} = 5000$ G with a ± 5.0 G oscillating field at frequencies in the range 0.6-10 kHz.

low activation energy-which could be more difficult to justify-by a direct relaxation process governed by the A parameter (see equation 8). The application of this new approach becomes more limited in the temperature range explored, but its results seem reasonable. The set of best-fit parameters through this approach are $E_{a1} = 42.0$ cm⁻¹, $\tau_{01} = 8.5 \times 10^{-8}$ s, $A = 930$ s⁻¹ K⁻¹, and $B = 4910$ s⁻¹.

$$\tau^{-1} = \tau_{01}^{-1} \exp(-E_{a1}) / kT + AT + B \quad (8)$$

The replacement of two-phonon Orbach process by a Raman relaxation (equation 9).

$$\tau^{-1} = CT^n + AT + B \quad (9)$$

led to very sensitive parameters with the frequency, and then it was finally discarded in this discussion. The negative D value obtained from the previous analysis of the experimental data or the theoretical study supports the presence of an energy barrier and the slow relaxation of the magnetization. Even further, the value of the energy barrier for the Orbach process (ca. 43 cm⁻¹) agrees with those extrapolated from the D value extracted from both the magnetometry and theory (46.6 and 40.4 cm⁻¹, respectively).

Conclusions

In summary, the reaction of a functionalized oxamate-type ligand with iron(II) (**1**), manganese(II) (**2**), zinc(II) (**3**) and copper(II) (**4**) afforded a high-spin mononuclear iron(II) complex (**1**), two isostructural uniform chains (**2** and **3**) and a dinuclear compound (**4**). Weak interchain antiferromagnetic interactions between manganese(II)

through hydrogen bonds occur in **2** whereas interdinuclear π - π stacking interactions are most likely responsible for the weak antiferromagnetic coupling between the copper(II) ions in **4**. Interestingly, compound **1** exhibits field-induced slow relaxation of the magnetization being the first reported example of a six-coordinate FeO₆ high-spin iron(II) complex showing the single-ion magnet (SIM) behavior. Its magnetostructural characterization has opened new windows towards the rational preparation of other examples of SIMs of six-coordinate high-spin iron(II) complexes that will be subject of future studies.

Supplementary Information

Crystallographic data (excluding structure factors) for the structures in this work were deposited in the Cambridge Crystallographic Data Centre as supplementary publication number CCDC 1869708, 1869709, 1869710, 1869711. Copies of the data can be obtained, free of charge, via www.ccdc.cam.ac.uk/conts/retrieving.html or from the Cambridge Crystallographic Data Centre, CCDC, 12 Union Road, Cambridge CB2 1EZ, UK; fax: +44 1223 336033. E-mail: deposit@ccdc.cam.ac.uk.

Supporting information for this article is available free of charge at <http://jbc.sbj.org.br> as PDF file.

Acknowledgments

This research was supported by the Ministério da Educação do Brasil for MCT/CNPQ (project Universal No. 409941/2016-6), CAPES/DGU (No. 295/13) and the Ministerio Español de Ciencia e Innovación through Projects CTQ2016-75068P and CTQ2016-75671P. J. W. M., L. K. and A. K. V. thank the CAPES and CNPq for grants as well as R. R. is grateful to Generalitat Valenciana. Thanks, are extended to the Spanish Consejo Superior de Investigaciones Científicas (CSIC) for the award of a license for the use of the Cambridge Structural Database (CSD).

References

- Lehn, J. M.; *Supramolecular Chemistry: Concepts and Perspectives*; VCH: Weinheim, Germany, 1995; *Transition Metals in Supramolecular Chemistry*, vol. 5; Sauvage, J. P., ed.; Wiley: New York, USA, 1999.
- Ferrando-Soria, J.; Vallejo, J.; Castellano, M.; Martínez-Lillo, J.; Pardo, E.; Cano, J.; Castro, I.; Lloret, F.; Ruiz-García, R.; Julve, M.; *Coord. Chem. Rev.* **2017**, *339*, 17.
- Pinkowicz, D.; Podgadny, R.; Nowicka, B.; Chorazy, S.; Reczyński, M.; Sieklucka, B.; *Inorg. Chem. Front.* **2015**, *2*, 10.
- Wang, X.-Y.; Avendaño, C.; Dunbar, K. R.; *Chem. Soc. Rev.* **2011**, *40*, 3213.
- Pedersen, K. S.; Bendix, J.; Clérac, R.; *Chem. Commun.* **2014**, *50*, 4396.
- Decurtins, S.; Pellaux, R.; Antorrena, G.; Palacio, F.; *Coord. Chem. Rev.* **1999**, *190-192*, 841.
- Pilkington, M.; Decurtins S.; *Oxalate-based 2D and 3D Magnets in Magnetism: Molecules to Materials II*; Miller, J. S.; Drillon M., eds.; Wiley VCH: Weinheim, 2001, p. 339.
- Gruselle, M.; Train, C.; Boubekur, K.; Gredin, P.; Ovanesyan, N.; *Coord. Chem. Rev.* **2006**, *250*, 2491.
- Martínez-Lillo, J.; Armentano, D.; de Munno, G.; Wernsdorfer, W.; Julve, M.; Lloret, F.; Faus, J.; *J. Am. Chem. Soc.* **2006**, *128*, 14218.
- Train, C.; Gheorghe, R.; Krstic, V.; Chamoreau, L.-M.; Ovanesyan, N. S.; Rikken, G. L. A.; Gruselle, M.; Verdaguer, M.; *Nat. Mater.* **2008**, *7*, 729.
- Marinescu, G.; Andruh, M.; Lloret, F.; Julve, M.; *Coord. Chem. Rev.* **2011**, *255*, 161.
- Clemente-León, M.; Coronado, E.; Martí-Gastaldo, C.; Romero, F. M.; *Chem. Soc. Rev.* **2011**, *40*, 473.
- Pardo, E.; Train, C.; Liu, H.; Chamoreau, L.-M.; Dkhil, B.; Boubekur, K.; Lloret, F.; Nakatani, K.; Tokoro, H.; Ohkoshi, S.-i.; Verdaguer, M.; *Angew. Chem., Int. Ed.* **2012**, *51*, 8356.
- Sadakiyo, M.; Okawa, H.; Shigematsu, A.; Ohba, M.; Yamada, T.; Kitagawa, H.; *J. Am. Chem. Soc.* **2012**, *134*, 5472.
- Martínez-Lillo, J.; Cañadillas-Delgado, L.; Cano, J.; Lloret, F.; Julve, M.; Faus, J.; *Chem. Commun.* **2012**, *48*, 9242.
- Martínez-Lillo, J.; Mastropietro, T. F.; Lhotel, E.; Paulsen, C.; Cano, J.; de Munno, G.; Faus, J.; Lloret, F.; Julve, M.; Nellutla, S.; Krzystek, J.; *J. Am. Chem. Soc.* **2013**, *135*, 13737.
- Martínez-Lillo, J.; Faus, J.; Lloret, F.; Julve, M.; Lloret, F.; Julve, M.; *Coord. Chem. Rev.* **2015**, *289-290*, 215.
- Mon, M.; Grancha, T.; Verdaguer, M.; Train, C.; Armentano, D.; Pardo, E.; *Inorg. Chem.* **2016**, *55*, 6845.
- Julve, M.; Gleizes, A.; Chamoreau, L.-M.; Ruiz, E.; Verdaguer, M.; *Eur. J. Inorg. Chem.* **2018**, 509.
- Ruiz, R.; Faus, J.; Lloret, F.; Julve, M.; Journaux, Y.; *Coord. Chem. Rev.* **1999**, *193-195*, 1069.
- Dul, M. C.; Pardo, E.; Lescouëzec, R.; Journaux, Y.; Ruiz-García, R.; Cano, J.; Julve, M.; Lloret, F.; Cangussu, D.; Pereira, C. L. M.; Stumpf, H. O.; Pasán, J.; Ruiz-Pérez, C.; *Coord. Chem. Rev.* **2010**, *254*, 2281.
- Journaux, Y.; Ferrando-Soria, J.; Pardo, E.; Ruiz-García, R.; Julve, M.; Lloret, F.; Cano, J.; Li, Y.; Lisnard, L.; Yu, P.; Stumpf, H.; Pereira, C. L. M.; *Eur. J. Inorg. Chem.* **2018**, 228.
- Cano, J.; Ruiz, E.; Alemany, P.; Lloret, F.; Alvarez, S.; *J. Chem. Soc., Dalton Trans.* **1999**, 1669.
- Grancha, T.; Ferrando-Soria, J.; Castellano, M.; Julve, M.; Pasán, J.; Armentano, D.; Pardo, E.; *Chem. Commun.* **2014**, *50*, 7569.

25. Castellano, M.; Ruiz-García, R.; Cano, J.; Ferrando-Soria, J.; Pardo, E.; Fortea-Pérez, F. R.; Stiriba, S.-E.; Barros, W. P.; Stumpf, H. O.; Cañadillas-Delgado, L.; Pasán, J.; Ruiz-pérez, C.; de Munno, G.; Armentano, D.; Journaux, Y. Lloret, F.; *Coord. Chem. Rev.* **2015**, *303*, 110.
26. Castellano, M.; Ruiz-García, R.; Cano, J.; Ferrando-Soria, J.; Pardo, E.; Fortea-Pérez, F. R.; Stiriba, S.-E.; Julve, M.; Lloret, F.; *Acc. Chem. Res.* **2015**, *48*, 510.
27. Grancha, T.; Ferrando-Soria, J.; Zhou, H.-C.; Gascon, J.; Seoane, B.; Pasán, J.; Fabelo, O.; Julve, M.; Pardo, E.; *Angew. Chem., Int. Ed.* **2015**, *54*, 6521.
28. Grancha, T.; Ferrando-Soria, J.; Cano, J.; Amorós, P.; Seoane, B.; Gascon, J.; Bazaga-García, M.; Losilla, E. R.; Cabeza, A.; Armentano, D.; Pardo, E.; *Chem. Mater.* **2016**, *28*, 4608.
29. Mon, M.; Pascual-Alvarez, A.; Grancha, T.; Cano, J.; Ferrando-Soria, J.; Lloret, F.; Gascon, J.; Pasán, J.; Armentano, D.; Pardo, E.; *Chem. Eur. J.* **2016**, *22*, 539.
30. Fortea-Pérez, F. R.; El Idrissi Moubtassim, M. L.; Armentano, D.; de Munno, G.; Julve, M.; Stiriba, S.-E.; *Inorg. Chem. Front.* **2018**, *5*, 2148.
31. Mon, M.; Adam, R.; Ferrando-Soria, J.; Corma, A.; Armentano, D.; Pardo, E.; Leyva-Pérez, A.; *ACS Catal.* **2018**, *8*, 10401.
32. Pardo, E.; Ruiz-García, R.; Lloret, F.; Faus, J.; Julve, M.; Journaux, Y.; Delgado, F.; Ruiz-Pérez, C.; *Adv. Mater.* **2004**, *16*, 1597.
33. Pardo, E.; Ruiz-García, R.; Lloret, F.; Faus, J.; Julve, M.; Journaux, Y.; Novak, M.; Delgado, F. S.; Ruiz-Pérez, C.; *Chem. Eur. J.* **2007**, *13*, 2054.
34. Fortea-Pérez, F. R.; Schlegel, I.; Julve, M.; Armentano, D.; de Munno, G.; Stiriba, S.-E.; *J. Organomet. Chem.* **2013**, *743*, 102.
35. Fortea-Pérez, F. R.; Marino, N.; Armentano, D.; de Munno, G.; Julve, M.; Stiriba, S.-E.; *CrystEngComm* **2014**, *16*, 6971.
36. Fortea-Pérez, F. R.; Armentano, D.; Julve, M.; de Munno, G.; Stiriba, S.-E.; *J. Coord. Chem.* **2014**, *67*, 4003.
37. Fortea-Pérez, F. R.; Rothenpieler, B. L.; Marino, N.; Armentano, D.; de Munno, G.; Julve, M.; Stiriba, S.-E.; *Inorg. Chem. Front.* **2015**, *2*, 1029.
38. Fortea-Pérez, F. R.; Neve, F.; Armentano, D.; de Munno, G.; Stiriba, S.-E.; Julve, M.; *Inorg. Chim. Acta* **2016**, *443*, 267.
39. Oliveira, T. L.; Kalinke, L. H. G.; Mascarenhas, E. J.; Castro, R.; Martins, F. T.; Sabino, J. R.; Stumpf, H. O.; Ferrando, J.; Julve, M.; Lloret, F.; Cangussu, D.; *Polyhedron* **2014**, *81*, 105.
40. Stumpf, H. O.; Pei, Y.; Kahn, O.; Sletten, J.; Renard, J. P.; *J. Am. Chem. Soc.* **1993**, *115*, 6738.
41. Fettouhi, M.; Ouahab, L.; Boudhari, A.; Cador, O.; Mathonière, C.; Kahn, O.; *Inorg. Chem.* **1996**, *35*, 4932.
42. Blay, G.; Fernández, I.; Pedro, J. R.; Ruiz-García, R.; Temporal-Sánchez, T.; Pardo, E.; Lloret, F.; Muñoz, M. C.; *J. Mol. Catal. A: Chem.* **2006**, *250*, 20.
43. Kumar, D.; Kapoor, I. P. S.; Singh, G.; Fröhlich, R.; *Thermochim. Acta* **2012**, *545*, 67.
44. Carlin, R. L.; *Magnetochemistry*; Springer-Verlag: Berlin, Germany, 1986.
45. Neese, F.; *Wiley Interdiscip. Rev.: Comput. Mol. Sci.* **2012**, *2*, 73.
46. Schafer, A.; Horn, H.; Ahlrichs, R.; *J. Chem. Phys.* **1992**, *97*, 2571.
47. Schafer, A.; Huber, C.; Ahlrichs, R.; *J. Chem. Phys.* **1994**, *100*, 5829.
48. Eichkorn, K.; Treutler, O.; Ohm, H.; Haser, M.; Ahlrichs, R.; *Chem. Phys. Lett.* **1995**, *240*, 283.
49. Eichkorn, K.; Treutler, O.; Ohm, H.; Haser, M.; Ahlrichs, R.; *Chem. Phys. Lett.* **1995**, *242*, 652.
50. Eichkorn, K.; Weigend, F.; Treutler, O.; Ohm, H.; Ahlrichs, R.; *Theor. Chem. Acc.* **1997**, *97*, 19.
51. *SADABS, APEX2 and SAINT*; Bruker AXS Inc., Madison, Wisconsin, USA, 2009.
52. Blessing, R. H.; *Acta Crystallogr., Sect. A: Found. Adv.* **1995**, *51*, 33.
53. Sheldrick, G. M.; *Acta Crystallogr., Sect. C: Struct. Chem.* **2015**, *71*, 3.
54. Macrae, C. F.; Bruno, I. J.; Chisholm, J. A.; Edgington, P. R.; McCabe, P.; Pidcock, E.; Monge, L. R.; Taylor, R.; van de Streek, J.; Wood, P. A.; *J. Appl. Crystallogr.* **2008**, *41*, 466.
55. Farrugia, L. J.; *J. Appl. Crystallogr.* **2012**, *45*, 849.
56. Pettersen, E. F.; Goddard, T. D.; Huang, C. C.; Couch, G. S.; Meng, E. C.; Ferrin, T. E.; *J. Comput. Chem.* **2004**, *25*, 1605.
57. Verdaguer, M.; Kahn, O.; Julve, M.; Gleizes, A.; *Nouv. J. Chim.* **1985**, *9*, 325.
58. Soto, L.; García, J.; Escrivá, E.; Legros, J. P.; Tuchagues, J. P.; Dahan, F.; Fuertes, A.; *Inorg. Chem.* **1989**, *28*, 3378.
59. Dey, S.; Sarkar, S.; Mukherjee, T.; Mondal, B.; Zangrando, E.; Sutter, J.-P.; Chattopadhyay, P.; *Inorg. Chim. Acta* **2011**, *376*, 129.
60. Vilela, R. S.; Oliveira, T. L.; Martins, F. T.; Ellena, J. A.; Lloret, F.; Julve, M.; Cangussu, D.; *C. R. Chimie* **2012**, *15*, 856.
61. Marinho, M. V.; Simões, T. R.; Ribeiro, M. A.; Pereira, C. L. M.; Machado, F. C.; Pinheiro, C. B.; Stumpf, H. O.; Cano, J.; Lloret, F.; Julve, M.; *Inorg. Chem.* **2013**, *52*, 8812.
62. Oxamide can be transformed into ammonium oxalate and oxalic acid by heating it for long periods with water; the best results are obtained under pressure. See: Riemenschneider, W.; Tanifuji, M. In *Ullmann's Encyclopedia of Industrial Chemistry*; Wiley-VCH: Weinheim, Germany, 2000; Du, M.; Zhang, Z.-H.; Li, C.-P.; Ribas-Ariño, J.; Aliaga-Alcaide, N.; Ribas, J.; *Inorg. Chem.* **2011**, *50*, 6850.
63. Simmons, E. L.; Wendlandt, W. W.; *Coord. Chem. Rev.* **1971**, *7*, 11.
64. Zuo, Y.G.; Hoigne, J.; *Environ. Sci. Technol.* **1992**, *26*, 1014.
65. Faust, D. C.; Zepp, R. G.; *Environ. Sci. Technol.* **1993**, *27*, 2517.
66. Nakamoto, K.; *Infrared Spectra of Inorganic and Coordination Compounds*, 4th ed.; Wiley: New York, 1986, p. 227.

67. Addison, A. V.; Rao, T. N.; Reedijk, J.; van Rijn, J.; Verschoor, G. C.; *J. Chem. Soc., Dalton Trans.* **1984**, 1349.
68. do Pim, W. D.; Simoes, T. R. G.; Oliveira, W. X. C.; Fernandes, I. R. A.; Pinheiro, C. B.; Lloret, F.; Julve, M.; Stumpf, H. O.; Pereira, C. L. M.; *Cryst. Growth Des.* **2014**, *14*, 5929.
69. Simoes, T. R. G.; do Pim, W. D.; Silva, I. F.; Oliveira, W. X. C.; Pinheiro, C. B.; Pereira, C. L. M.; Lloret, F.; Julve, M.; Stumpf, H. O.; *CrystEngComm* **2013**, *15*, 10165.
70. Wang, Q.-L.; Liao, D.-Z.; Yan, S.-P.; Jiang, Z.-H.; Cheng, P.; *Chin. J. Chem.* **2002**, *20*, 1249.
71. Groom, C. R.; Bruno, I. J.; Lightfoot, M. P.; Ward, S. C.; *Acta Crystallogr., Sect. B: Struct. Sci., Cryst. Eng. Mater.* **2016**, *72*, 171.
72. Conte-Daban, A.; Borghesani, V.; Sayen, S.; Guillon, E.; Journaux, Y.; Gontard, G.; Lisnard, L.; Hureau, C.; *Anal. Chem.* **2017**, *89*, 2155.
73. Bleaney, B.; Bowers, K. D.; *Proc. R. Soc. London, Ser. A* **1952**, *214*, 451.
74. Girerd, J. J.; Charlot, M. F.; Kahn, O.; *Mol. Phys.* **1977**, *34*, 1063.
75. Kahn, O.; Charlot, M. F.; *Nouv. J. Chim.* **1980**, *4*, 567.
76. Desplanches, C.; Ruiz, E.; Rodríguez-Fortea, A.; Alvarez, S.; *J. Am. Chem. Soc.* **2002**, *124*, 5197.
77. Desplanches, C.; Ruiz, E.; Alvarez, S.; *Chem. Commun.* **2002**, 2614.
78. Bertrand, J. A.; Black, T. D.; Eller, P. G.; Helm, F. T.; Mahmood, R.; *Inorg. Chem.* **1976**, *15*, 2965.
79. de Munno, G.; Ventura, V.; Viau, G.; Lloret, F.; Faus, J.; Julve, M.; *Inorg. Chem.* **1998**, *37*, 1458.
80. Cano, J.; *VPMAG*; University of Valencia, Valencia, Spain, 2003.
81. Mabbs, F. E.; Machin, D. J.; *Magnetism and Transition Metal Complexes*; London Chapman and Hall: London, 1973, p. 160.
82. Kahn, O.; *Molecular Magnetism*; VCH Wiley: New York, 1993.
83. Zadrovny, J. M.; Atanasov, M.; Bryan, A. M.; Lin, C.-Y.; Rekken, B. D.; Power, P. P.; Neese, F.; Long, J. R.; *Chem. Sci.* **2013**, *4*, 125.
84. Li, H.-P.; Smythe, N. C.; Gorelsky, S. I.; Maguire, S.; Henson, N.; Korobkov, I.; Scott, B. L.; Gordon, J. C.; Baker, R. T.; Murugesu, M.; *J. Am. Chem. Soc.* **2011**, *133*, 15806.
85. Freedman, D. E.; Harman, W. H.; Harris, T. D.; Long, G. J.; Chang, C. J.; Long, J. R.; *J. Am. Chem. Soc.* **2010**, *132*, 1224.
86. Harman, W. H.; Harris, T. D.; Freedman, D. E.; Fong, H.; Chang, A.; Ozarowski, A.; Rinehart, J. D.; Sougrati, M. T.; Grandjean, F.; Long, G. J.; Long, J. R.; Chang, C. J.; *J. Am. Chem. Soc.* **2010**, *132*, 18115.
87. Mathonière, C.; Lin, H.-J.; Sirenatu, D.; Clérac, R.; Smith, J. M.; *J. Am. Chem. Soc.* **2013**, *135*, 19083.
88. Weismann, D.; Sun, Y.; Lan, Y.; Wolmershäuser, G.; Powell, A.; Sitzmann, H.; *Chem. Eur. J.* **2011**, *17*, 4700.
89. Feng, X.; Mathonière, C.; Jeon, I.-R.; Rouzières, M.; Ozarowski, A.; Aubrey, M. L.; Gonzalez, M. I.; Clérac, R.; Long, J. R.; *J. Am. Chem. Soc.* **2013**, *135*, 15880.
90. Shao, D.; Zhao, X.-H.; Zhang, S.-L.; Wu, D.-Q.; Wei, X.-Q.; Wang, X.-Y.; *Inorg. Chem. Front.* **2015**, *2*, 846.
91. Bar, A. K.; Pichon, C.; Gogoi, N.; Duhayon, C.; Ramasesha, S.; Sutter, J.-P.; *Chem. Commun.* **2015**, *51*, 3616.
92. Xiang, J.; Liu, J.-J.; Chen, X.-X.; Jia, L.-H.; Fu, Y.; Wang, B.-W.; Gao, S.; Lau, T.-C.; *Chem. Commun.* **2017**, *53*, 1474.
93. Li, G.-L.; Wu, S.-Q.; Zhang, L.-F.; Wang, Z.; Ouyang, Z.-W.; Ni, Z.-H.; Su, S.-Q.; Yao, Z.-S.; Li, J.-Q.; Sato, O.; *Inorg. Chem.* **2017**, *56*, 8018.

Submitted: February 1, 2019

Published online: July 12, 2019

Additions and Corrections

Page 2416, Table 1, column denominated “2”:

Where it reads	Should be read
0.952	1.073

Page 2416, Table 1, column denominated “3”:

Where it reads	Should be read
9.9959(15)	11.4598(4)
12.6546(18)	7.2430(3)
77.108(10)	27.8592(8)
88.005(10)	90
87.143(9)	90
1002.2(3)	90
5004	5002
1890	1888
92.6	92.5
1.137	1.130

J. Braz. Chem. Soc., Vol. 31, No. 12, 2651-2652, 2020.<https://dx.doi.org/10.21577/0103-5053.20200198>